AN ABSTRACT OF THE THESIS OF

Haley Cynar for the degree of Master of Science in Ocean, Earth and Atmospheric Sciences presented on February 3, 2021.

Title: High-resolution Biological Net Community Production in the Pacific-influenced Arctic: A Multi-method Comparison

Abstract approved:

_____

Lauren Juranek

Patterns of primary productivity in the Arctic are expected to change with continued warming, yet productivity measurements are historically limited, both spatially and temporally. An established method of measuring net biological oxygen production, which can be used to estimate net community production (NCP) rates, is with an equilibrated inlet mass spectrometer (EIMS) that measures oxygen to argon ratios (O_2/Ar) in underway seawater. An emerging method that may provide comparable estimates of biological oxygen production involves a gas tension device (GTD) coupled with an optode, which yields oxygen to nitrogen ratios (O_2/N_2). The GTD+optode combination is small, inexpensive, and capable of autonomous deployments on ships, moorings, and other surface platforms; however, the dissimilarity in gas solubility between O_2 and N_2 makes this tracer pair less favorable than O_2/Ar. We conducted a side-by-side comparison of a GTD and EIMS during the 2019 Arctic Integrated Ecosystem Survey OS1901-L1 in the Pacific Arctic. We found that O_2/Ar and O_2/N_2 tracked each other closely, with small differences due to physical drivers of deviations between O_2/Ar and O_2/N_2, including wind and

temperature changes. The NCP estimates from O_2/N_2 were generally consistent with O_2/Ar-based NCP estimates observed on this cruise, with median NCP from O_2/Ar and O_2/N_2 of 7.49 ± 2.34 and 7.16 ± 2.68 mmol O_2 m^{-2} day^{-1}, respectively, suggesting the GTD-based method can be used to enhance spatial and temporal coverage of NCP measurements. However, the GTD/optode approach is reliant on well-calibrated oxygen observations, which may present a challenge in some cases.

High-resolution Biological Net Community Production in the Pacific-influenced Arctic: A Multi-method Comparison

by
Haley Cynar

A THESIS

submitted to

Oregon State University

in partial fulfillment of
the requirements for the
degree of

Master of Science

Presented February 3, 2021
Commencement June 2021

Master of Science thesis of Haley Cynar presented on February 3, 2021

APPROVED:

Major Professor, representing Ocean, Earth and Atmospheric Sciences

Dean of the College of Earth, Ocean and Atmospheric Sciences

Dean of the Graduate School

I understand that my thesis will become part of the permanent collection of Oregon State University libraries. My signature below authorizes release of my thesis to any reader upon request.

Haley Cynar, Author

ACKNOWLEDGEMENTS

I would like to thank my advisor, Laurie Juranek, for her support and guidance throughout this research. Without her mentorship and thorough comments throughout the writing process, this thesis would not be possible. I would like to thank my committee members for the support, encouragement, and ideas that have been instrumental in my path here. I would also like to acknowledge my cohort, officemates, and friends who have made these past years full of adventures.

CONTRIBUTION OF AUTHORS

L.W.J. and C.W.M contributed to the study's conception. H.C. and D.S. contributed to data acquisition. H.C. analyzed the data and wrote the initial draft of the paper. H.C., L.W.J. and C.W.M contributed to development of the paper. C.W.M. provided resources. H.C., L.W.J., C.W.M and D.S. approved the final manuscript.

TABLE OF CONTENTS

LIST OF FIGURES

LIST OF TABLES

Table Page

1 Introduction

The Arctic Ocean is changing at an unprecedented rate: the thirteen lowest minimum sea ice extents in the satellite record have all occurred between 2007 and 2020, while the trend in September sea ice extent has been declining by 13.3% per decade over the period 1979-2014, relative to the mean September sea ice extent from 1981-2010 (Serreze and Stroeve 2015; Stroeve and Meier 2018; Andersen et al. 2020). In some of the most impacted regions of the Arctic Ocean, including the Chukchi and western Beaufort seas, the ice season duration has been declining by an average of 2.8 days per year from 1979/1980 to 2010/2011 (Stammerjohn et al. 2012). This particularly rapid decline in sea ice impacts the physical environment in many ways: increased exchange of heat and gases (CO_2) across the air-sea boundary (Anderson and Kaltin 2001; Carmack et al. 2015; DeGrandpre et al. 2020), enhanced wind fetch across open water that results in greater waves and vertical mixing, and greater stratification from low-salinity meltwater. Stronger stratification limits vertical mixing, which in turn limits surface nutrient supply, a fundamental requirement for photosynthesis (Semiletov et al. 2004; Carmack and Wassmann 2006).

While the Arctic Ocean is rapidly changing, the magnitude and direction of change in primary productivity is uncertain, with hypotheses for both increasing and decreasing production based on nutrient and light availability. Increased production has been observed by remote sensing, which has been hypothesized to be associated with sea ice loss and reduction in light limitation (Arrigo et al. 2008; Tremblay et al. 2011; Arrigo and van Dijken 2015). However, recent remote

sensing analysis suggests that these productivity increases might have been sustained by an increase in nutrient input from adjacent subpolar seas, which most directly impacts inflow shelves like the Chukchi Sea (Lewis et al. 2020). Alternatively, potential increases in cloud cover are expected to decrease production (Bélanger et al. 2013), while increased delivery of freshwater and dissolved constituents from terrestrial snow, ice, and permafrost melt via Arctic rivers will impact nutrients, stratification, and organic matter in coastal regions with variable results (Carmack and Wassmann 2006). Overall, a melting Arctic Ocean will alter surface light and nutrient availability, effectively controlling phytoplankton growth, a factor that impacts carbon and energy cycling in Arctic marine food webs (Grebmeier et al. 2006; Harada 2016).

Remote sensing approaches for estimating marine productivity have the potential to provide spatially and temporally resolved data, but these measurements are often limited in the Arctic due to cloud cover, especially during the late ice-free season (August-October) when physical system changes are maximal. Field-based observations of productivity are still needed to calibrate and validate remote sensing algorithms and to identify or confirm mechanisms supporting enhanced growth. Incubation-based studies (Quay et al. 2012; Ducklow and Doney 2013) are the most commonly used field-based approach for constraining marine productivity. However, these discrete measurements are time- and labor-intensive, have unknown uncertainties due to bottle effects, and are inevitably limited in quantity and spatial/temporal scope. Since biological productivity in shallow, marginal seas like the Chukchi is dynamic, often with patchy and short-lived phytoplankton blooms (Juranek et al. 2019), this region in particular

would benefit from a higher resolution method to capture sporadic and spatially-variable processes.

One important productivity metric that is especially useful with regard to evaluating production fueled by new nutrient sources is net community production (NCP), a measure of the balance between photosynthesis and respiration. NCP is defined as the total amount of photosynthesis minus both algal and heterotrophic respiration, and is considered to be a measure of the total carbon available to be exported out of the surface ocean or consumed by higher trophic levels, with implications for the ecosystem, fisheries, carbon budgets, and climate modeling (Wassmann and Reigstad 2011). NCP is often also equated with new production, the production fueled by inorganic nutrient supply, under steady state conditions (Eppley and Peterson 1979).

An established method of obtaining high-resolution measurements of NCP is by measuring the ratio of dissolved oxygen to argon (O_2/Ar) continuously in surface seawater using an equilibrated inlet mass spectrometer (EIMS) (Cassar et al. 2009). Since argon is an inert gas that is not affected by biology, the ratio of biologically and physically controlled oxygen to physically controlled argon, O_2/Ar, provides a measure of net biological oxygen production (Benson and Krause 1984; Craig and Hayward 1987). The O_2/Ar ratio is insensitive to changes in dissolved gases such as warming, cooling, and wind-driven bubble exchange and injection due to the similarity in physical properties between oxygen and argon. When O_2/Ar measurements are combined with a simple steady state mass-balance budget for the surface ocean, spatially

resolved estimates of NCP can be produced (Stanley et al. 2010; Hamme et al. 2012; Eveleth et al. 2017).

Another related, but less frequently used approach for obtaining NCP is to use observations of the O_2/N_2 ratio in seawater. Similar to the case with O_2/Ar, N_2 is used to track abiotic forcing, where N_2 acts as a tracer of physical saturation changes in a similar way to Ar. While O_2 and Ar are an ideal tracer pair due to the similar solubility of these gases, N_2 is less similar to O_2 and is impacted differently by both physical forcing and, at times, biological influences. The O_2/N_2 method was previously described by Emerson et al. (2002), who used observations from an O_2 optode and a gas tension device (GTD) mounted on a mooring near the Hawaii Ocean Time-series study site in the subtropical North Pacific to estimate net biological oxygen production. The approach involves measuring total gas pressure in seawater with a GTD, and use of O_2 concentrations in concert with assumptions about less prevalent gases to estimate the amount of dissolved N_2. Because of the reliance on O_2 to calculate N_2, the approach requires accurate dissolved O_2 concentrations (Emerson et al., 2002).

While O_2/N_2-based net biological oxygen estimates are subject to greater biases and uncertainties due to the differing physical forcing of O_2 and N_2, there are also key advantages to the approach. The GTD/optode system is small, submersible, and low-cost, with potential for autonomous use, whereas the EIMS involves a more expensive, ship-based mass spectrometer that requires supervision. Here, we compare underway O_2/N_2 to the more established O_2/Ar method (Stanley et al. 2010; Hamme et al. 2012; Lockwood et al. 2012; Eveleth et al. 2014) to evaluate the

effectiveness of this approach for autonomous underway applications. The differences in these approaches during a summer 2019 research cruise in the Bering and Chukchi Seas will be assessed alongside estimates of physical forcing along the cruise track to identify whether physical factors (temperature change, bubble injection) were responsible for biasing the O_2/N_2 measurements, and to assess the overall utility of O_2/N_2 in estimating net biological oxygen production and NCP in this region of the Pacific Arctic.

2 Methods

In this study, EIMS- and GTD- based estimates of NCP were obtained for a side-by-side comparison on leg 1 of the OS1901 cruise on R/V *Ocean Starr*, August 1 to August 24, 2019. The cruise (OS1901-L1) was a part of the Arctic Integrated Ecosystem Survey in the Chukchi and Beaufort Seas.

2.1 Dissolved O_2 measurements

An Aanderaa optode (4330F) was placed in-line with the GTD in the flow through seawater system, which had an intake depth of 3.5 meters. Discrete Winkler oxygen samples were collected periodically throughout the cruise (n=26), and analyzed using a Winkler approach (Carpenter 1965) in order to calibrate the sensor-based O_2 data. Upon inspection, 5 of these samples were determined to be outliers, as determined by either residing outside two standard deviations from the mean offset or being analyzed in a batch of samples that were subject to analysis error, and were excluded from further analysis. Offsets between Winkler and optode measurements were determined with respect to time, temperature, and oxygen concentration, where the best fit linear model of the difference in offset as a function of temperature was applied to the data, with a correlation coefficient of 0.95. This temperature-based offset correction ranged from 10-20 µmol/kg and is described in the metadata accompanying this data set.

2.2 EIMS-O_2/Ar

An equilibrated inlet mass spectrometer (EIMS), which consists of a quadrupole mass spectrometer (Pfeiffer PrismaPlus QMG 220) coupled to a system for separation of dissolved gases from seawater, was configured similarly to that described by Cassar et al. (2009). O_2/Ar ratios were continuously measured on surface seawater by the EIMS, where seawater passed through a 40 mesh (0.42 mm) coarse screen, followed by 100 and 5 µm filters before entering an overflowing cylinder in a sipper system. Seawater near the inflow of this cylinder was pumped through a contactor membrane (3M Liqui-cel MicroModule 0.75 x 1, model G569) with large surface area in which dissolved gases equilibrated. The headspace of gas in this contactor membrane was sampled by a fused silica capillary (2 m x .05 mm ID) connected to the quadrupole mass spectrometer. A changeover valve allowed outside air to be admitted for 30 minutes every 3 hours. O_2/Ar in ambient air is considered to be constant, so consistent air measurements throughout the cruise allows for calibration of the seawater O_2/Ar signal to air O_2/Ar to account for potential drift in EIMS measurements over time.

The EIMS O_2/Ar ratios were time-averaged into 2.5-minute intervals to yield measurements with average spatial resolution of ca. 0.6 km along the ship transit, that were then corrected to air O_2/Ar. These O_2/Ar measurements were aligned to the optode O_2 measurements to correct for a time delay in the EIMS measurement due to equilibration and capillary transport time. Using a cross-correlation analysis, a lag of 8.5 minutes was identified, and the EIMS measurements were adjusted accordingly to align with the faster response optode data. Bottle samples were collected

from the underway seawater stream twice a day and analyzed via a shore-based Thermo 253 Isotope Ratio Mass Spectrometry (IRMS) as in Juranek et al. (2012). Bottle samples were used as a secondary, external accuracy check on air corrected EIMS O_2/Ar. Outliers in the bottle calibrations (defined as outside 3 standard deviations of the mean difference) were observed in frontal regions of rapid O_2/Ar ratio change, and were excluded from the offset determination because small differences in sampling response time allowed for large offsets that were inconsistent with the majority of the data. Bottle and EIMS O_2/Ar data were used with paired temperature and salinity to calculate the O_2/Ar saturation (ΔO_2/Ar) as follows:

$$\Delta O_2/Ar = 100*[(O_2/Ar)_{meas}/(O_2/Ar)_{sat}-1], \quad (1)$$

where $(O_2/Ar)_{sat}$ refers to the ratio of gases at saturation in seawater at 1-atm pressure of air, and O_2 and Ar solubilities are calculated according to Garcia and Gordon (1992) and Hamme and Emerson (2004), respectively.

There was an overall offset in ΔO_2/Ar of -1.33 % (n=34, s.e.m.=0.1%) for EIMS ratios to discrete bottles, and this correction was applied to the EIMS data as a total offset. See metadata description accompanying archived data for further details.

2.3 GTD-O_2/N_2

The Pro-Oceanus miniTDGP (referred to as GTD) was installed on the flow through seawater system to measure total dissolved gas pressure of surface seawater throughout the cruise. This device measures the total dissolved gas pressure across a permeable membrane twice per second. The flow rate of seawater entering the GTD was about 1.2 L min^{-1}, producing a relatively fast response time in the sensor when compared to the EIMS response time. Since this configuration was set up directly in line with the underway seawater (in contrast to the EIMS with a sipper), these measurements were subject to greater noise at times due to bubbles in the seawater line.

The GTD measures total dissolved gas pressure in seawater ($P^w_{GTD,}$) expressed as in Equation 2,

$$P^w_{GTD} = P^w_{N2} + P^w_{O2} + P^w_{H20} + P^w_{Ar} + P^w_{CO2} \quad (2)$$

where P^w_x refers to the partial pressure of dissolved N_2, O_2, water vapor, Ar, and CO_2 in seawater, respectively. This expression excludes gases with partial pressures less than 20 µatm, which Emerson et al. (2002) showed was a reasonable assumption. P^w_{Ar}, P^w_{CO2}, and P^w_{H2O} are assumed to be at equilibrium with the atmosphere, an assumption that is likely inaccurate, yet expected deviations in these gas concentrations will not strongly affect the calculation due to the small contribution of each of these gases to total dissolved gas pressure. The dry air mole fraction of CO_2 in the atmosphere was used in this calculation, where the monthly average pCO_2 in August 2019 at the Point Barrow, AK climate monitoring station was 400 ppm (NOAA

CMDL, https://www.esrl.noaa.gov/gmd/dv/data/). The partial pressure of CO_2 and Ar were calculated based on the mole fraction of each gas in the atmosphere with the relationship in Equation 3:

$$P^a_i = X_i * (P^a - P^a_{H20}) \quad (3)$$

where P^a_i is the partial pressure of gas (i=CO_2 or Ar), X_i is the fraction of gas in a dry atmosphere, P^a is the atmospheric pressure and P^a_{H2O} is the partial pressure of water vapor in the atmosphere (Glueckauf 1951). P^w_{H2O} is assumed to be at saturation in the surface ocean and is calculated with the formula of Weiss and Price (1980). Daily atmospheric pressure (P^a) at mean sea level along the cruise track was determined from NCEP North American Regional Reanalysis (NARR) data provided by the NOAA/OAR/ESRL PSL (Mesinger et al. 2006), Boulder, Colorado, USA (https://psl.noaa.gov/).

To calculate the partial pressure of dissolved oxygen, a solubility constant, α_{O2}, was calculated with units of mol kg^{-1} atm^{-1} as follows:

$$\alpha_{O2} = [O_2]_{sat} / (P^a - P^a_{H2O}) * X_{O2} \quad (4)$$

where the equilibrium saturation concentration of oxygen at each location, $[O_2]_{sat}$, was determined based on the equations of Garcia and Gordon (1992). As above, P^a is atmospheric pressure and P^a_{H2O} is the partial pressure of water vapor in the atmosphere (assumed to be at

saturation) and X_{O2} is the mole fraction of O_2 in a dry atmosphere (Glueckauf 1951). This solubility constant, α_{O2}, was then used to calculate the partial pressure of O_2 in the water vapor-saturated headspace of the GTD as in Equation 5,

$$P^w_{O2} = [O_2]_{meas}/\alpha_{O2} \quad (5)$$

where $[O_2]_{meas}$ is the concentration of O_2 measured by the optode, in mol/kg.

The P^w_{N2} can then be calculated as (Emerson et al. 2002):

$$P^w_{N2} = P^w_{GTD} - (P^a - P^a_{H20})*(X_{Ar} + X_{CO2}) - P^w_{H20} - [O_2]_{meas}/\alpha_{O2}; \quad (6)$$

The P^w_{GTD} data were corrected via subtraction for a 6.5-minute time lag (determined via a cross-correlation analysis) relative to the faster response Aanderaa optode data. From P^w_{N2} and P^w_{O2} as calculated post P^w_{GTD} lag correction, measured O_2/N_2 ratios were determined.

We report O_2/N_2 here in terms of a saturation ratio comparable to Equation 1:

$$\Delta O_2/N_2\ (\%) = 100*[\ (O_2/N_2)_{meas}/(O_2/N_2)_{sat} - 1] \quad (7)$$

where $(O_2/N_2)_{sat}$ refers to the ratio of gases at saturation in equilibrium with the GTD headspace as calculated by Equation 5 or 6. The gas solubilities are calculated from Garcia and Gordon (1992) and Hamme and Emerson (2004). In calculating the O_2/N_2 ratio, a median residual filter

was applied to the raw gas pressure data to remove outliers and noise due to in-line bubbles, see metadata description accompanying archived data for further details.

The O_2/N_2 method has previously been used for O_2/N_2-based net biological oxygen production estimates on moorings in the subtropical North Pacific and Southern Ocean (Emerson et al. 2002, 2008; Weeding and Trull 2014; Trull et al. 2019), while continuous shipboard GTD measurements have been made in the northwest Atlantic (McNeil et al. 2005). Recently, Izett and Tortell (2020) introduced a GTD and optode configuration (Pressure of In Situ Gases Instrument, or PIGI) for deployment on underway systems, with initial data collection in the northeast Pacific and Canadian Arctic oceans.

2.4 Gas Ratio Comparison

The dissolved gas saturation of oxygen in the surface ocean

$$\Delta O_2\,(\%) = 100*([O_2]_{meas}/[O_2]_{sat} - 1) \quad (8)$$

gives an indication of the net balance of biological production and respiration, but this signal is also convoluted by abiotic factors (warming, cooling, bubble injection). For example, a recent water column warming of 3°C (e.g. from 10° to 13° C) without sufficient time for re-equilibration with the atmosphere would increase ΔO_2 by 6.57% due to the decrease in solubility of O_2 ($[O_2]_{sat}$) with increasing temperature. A positive gas saturation could also be driven by a

source of O_2 (i.e. photosynthesis), which increases $[O_2]_{meas}$. Without an additional tracer gas, it is difficult to identify when positive ΔO_2 are driven by biological production or a combination of physical factors. By simultaneously measuring an abiotic gas such as Ar or N_2 as a tracer of physical saturation changes, the physical and biological components of the ΔO_2 signal can be parsed out. Ar has been widely used as an abiotic tracer alongside O_2 because it is inert and is physically similar to oxygen (Craig and Hayward 1987).

Although N_2 has biological sources and sinks, the effect of these processes are typically assumed to be undetectable given the large N_2 background in surface measurements, making N_2 an effective tracer of physical processes (Emerson et al. 2002). In the Bering and Chukchi seas, the rate of nitrogen fixation is inconsequential with respect to surface N_2 concentrations (Harding et al. 2018; Shiozaki et al. 2018), yet denitrification in bottom water and sediment yields elevated dissolved nitrogen gas that may measurably change N_2 in the surface mixed layer when vertical mixing occurs (Mordy et al., submitted), the effect of which is estimated later with respect to $\Delta O_2/N_2$. With Ar and N_2 serving as proxies for physical gas saturation, the normalization of ΔO_2 relative to either gas yields a tracer of the net biological oxygen saturation. Biological O_2 production can be stoichiometrically related to the net inventory of organic carbon produced through the balance of community photosynthesis and respiration, i.e.: $CO_2 + H_2O \leftrightarrow$ organic matter + O_2. As is evident from this expression, net biological oxygen increases due to photosynthesis and decreases due to respiration for a given parcel of water.

However, the physical differences between N_2 and O_2 are significantly greater than those between Ar and O_2, so physical forcing (for example warming or cooling of water masses) is expected to drive slightly different responses in O_2 and N_2, and hence the O_2/N_2 ratio will not be a perfect tracer of net biological O_2 production. Since N_2 makes up 78% of the atmosphere (Glueckauf 1951) yet is less soluble in seawater than either O_2 or Ar, the effect of bubble injection increases N_2 saturation significantly more than O_2 or Ar. The effect of temperature change on N_2, in contrast, is smaller than that of O_2 and Ar, which also biases the ratio when temperature change is observed. To observe and assess the comparison between these gas ratios, we calculate their difference as the term diff-Δ:

$$\text{diff-}\Delta\ (\%) = \Delta O_2/Ar - \Delta O_2/N_2 \quad (9)$$

In order to compare GTD-based O_2/N_2 to EIMS-based O_2/Ar, we must first account for differences in the dynamic response of each instrument. The EIMS equilibrator, a contactor membrane, dampens signals due to the time required for gases to reach equilibrium across the membrane. When calculating diff-Δ, this difference in time responses between instruments creates large data artifacts due to the mismatched peaks. To account for the smearing of signals within the EIMS equilibrator, a smoothed version of $\Delta O_2/N_2$ was calculated for use in comparing the two ratios. A one-sided exponential filter with an e-folding time of 7.75 minutes (the e-folding time determined by Cassar et al. 2009 for a comparable EIMS configuration) was applied over three time periods to the total dissolved gas pressure measurements to simulate the smoothing effect of the EIMS contactor membrane, which is referred to as $\Delta O_2/N_{2smoothed}$. After

applying this filter, the gas pressure signal was aligned with the optode and averaged into bins corresponding to those of O_2/Ar from the EIMS, see metadata description accompanying archived data for further details.

2.5 NCP Calculation

Net community production (NCP) was calculated for ΔO_2/Ar and $\Delta O_2/N_2$ values by assuming a steady state balance between net biological oxygen production and air-sea gas exchange in the surface mixed layer with no horizontal advection or vertical mixing of water masses (Craig and Hayward 1987; Kaiser et al. 2005; Hamme and Emerson 2006; Stanley et al. 2010). When there is physical transport of deeper water to the surface and mixing assumptions are invalidated it is not appropriate to calculate NCP using the steady-state balance (Teeter et al. 2018). Diagnosing potential mixing biases using only surface underway data can be challenging, but some characteristics of deeper water that may indicate vertical mixing in the region of this study include elevated salinity coupled with negative ΔO_2/Ar at the surface, since subsurface waters are typically depleted in oxygen at depth due to respiration, and their salinity is higher due to minimal influence of seasonal ice melt at depth. In this dataset, areas with both a ΔO_2/Ar less than -2% and a surface salinity greater than 32.5 are assumed to be subject to vertical mixing, and are excluded from NCP calculations.

NCP was calculated using Equation 10 with NCP in mmol O_2 m^{-2} day^{-1}:

$$NCP=(k_{O2})(O_2)_{sat}(\Delta O_2/[X])/100, \quad (10)$$

In Equation 10, k_{O2} is the air-sea gas exchange rate (m day^{-1}), $(O_2)_{sat}$ is the equilibrium saturation of oxygen calculated as described above (mmol m^{-3}), and $\Delta O_2/[X]$ is either $\Delta O_2/Ar$ or $\Delta O_2/N_2$ as calculated with Equation 1 or 7. The gas transfer velocity, k_{O2}, is dependent on wind speed and was calculated based on Wanninkhof (2014) using the wind speed weighting technique of Reuer et al. (2007). Daily average directional components of wind speed from NCEP North American Regional Reanalysis (NARR) provided by the NOAA/OAR/ESRL PSL, Boulder, Colorado, USA were used in calculating the gridded wind speed for the 60 days prior to ship observations. (https://psl.noaa.gov/).

2.6 Variables to Assess Physical Gas Saturation

In order to evaluate potential variables that might corelate with differences in gas ratios, we compare remotely sensed wind speed and temperature to diff-Δ. The average squared wind speed over two weeks prior to sampling was calculated based on the NARR wind speed data described above. This parameter is expected to correspond to bubble effects, as the value is proportional to the wind speed-bubble injection approximation of Woolf and Thorpe (1991). Cumulative temperature change was calculated as the sum of daily sea surface temperature (SST) change two weeks prior to sampling, using NOAA High-resolution Blended Analysis of Daily SST and Ice data *provided by the NOAA/OAR/ESRL PSL, Boulder, Colorado, USA, from (*https://psl.noaa.gov/).

3 Results and Discussion

3.1 A simple theoretical model to simulate gas ratio differences

Differences in $\Delta O_2/Ar$ and $\Delta O_2/N_2$, referred to as diff-Δ, are expected due to a variety of physical factors including gas solubility, bubble injection, and gas exclusion principles. For example, an increase in temperature instantaneously changes the gas solubility in the water mass; the solubility of both argon and oxygen will change similarly due to their comparable solubility, while nitrogen solubility decreases to a lesser extent because it is less soluble. This difference in temperature effect between N_2 and Ar appears small in the individual gas saturation anomalies (Figure 1A), but becomes amplified when calculating gas ratios due to the dissimilarity between N_2 and O_2. The result is an $\Delta O_2/N_2$ ratio change that is 12 times greater than $\Delta O_2/Ar$ due to

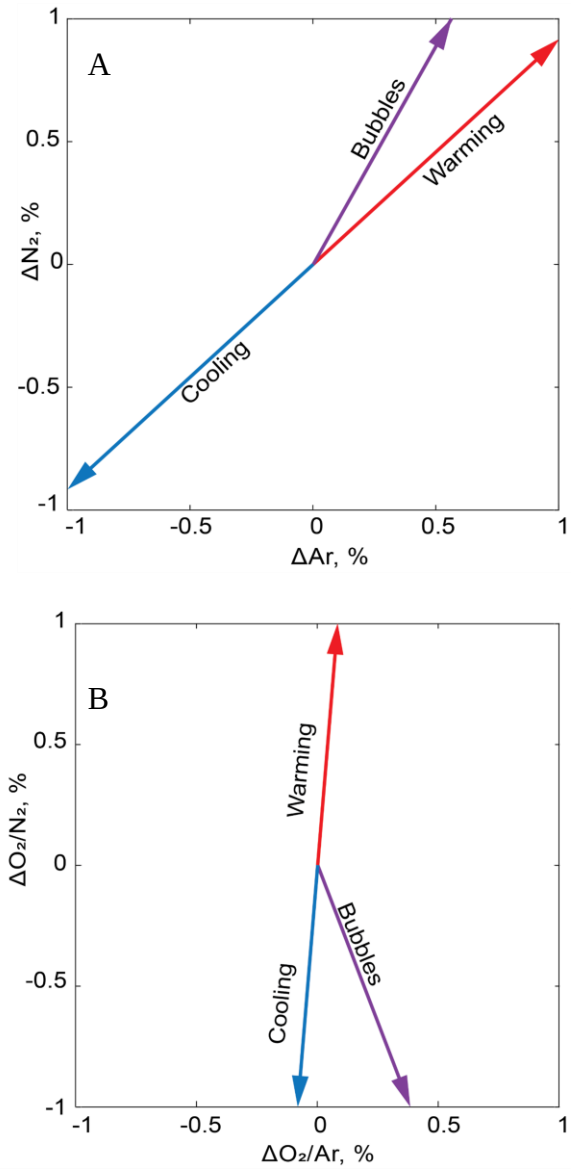

Figure 1: Expected changes in ΔAr, ΔN_2, $\Delta O_2/Ar$ and $\Delta O_2/N_2$ due to temperature change and bubble injection.

these solubility differences (Figure 1B). For example, a recent warming of 3°C would result in an increase in O_2, N_2, and Ar saturations of 6.57%, 5.93%, and 6.51% respectively, but a diff-Δ ($\Delta O_2/Ar$ - $\Delta O_2/N_2$) of -0.52% (i.e., $\Delta O_2/Ar$ =0.08%, $\Delta O_2/N_2$=0.60%). This warming-induced saturation signal will erode via exchange with the atmosphere over subsequent weeks as the upper ocean re-equilibrates to the new temperature.

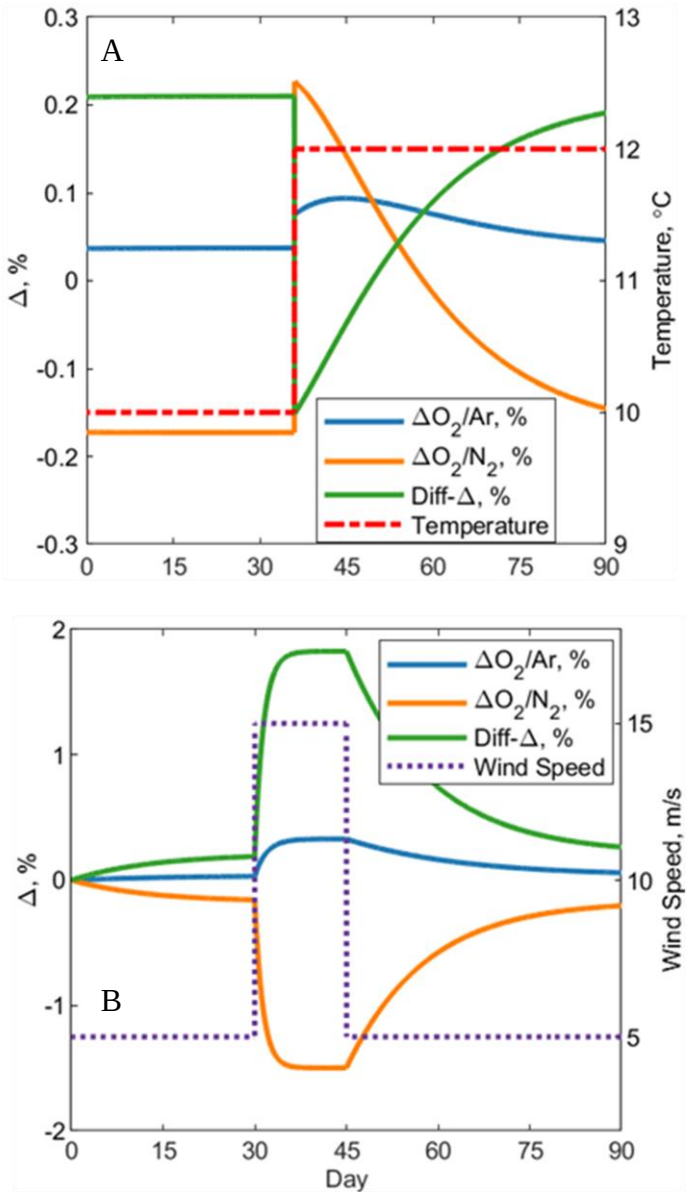

Figure 2: Box model of gas saturation change in $\Delta O_2/Ar$ and $\Delta O_2/N_2$ with (A) warming water and (B) increased wind speed. Baseline parameters include a mixed layer depth of 20 meters, temperature of 10°C, salinity of 32 and wind speed of 5 m/s.

Conversely, wind-driven bubble injection creates a gas supersaturation due to enhanced gas injection which increases over the period of enhanced wind. Bubble injection and bubble exchange, parameterized as wind-driven based on the equations of Woolf and Thorpe (1991), will increase individual gas saturations but will decrease the $\Delta O_2/N_2$ ratio due to the high mole fraction of N_2 in the

atmosphere and the relatively low solubility of N_2 in seawater. The wind-driven supersaturation of N_2 is much larger than the supersaturation of more soluble gases (O_2, Ar), such that enhanced wind will increase diff-Δ. If wind speed increases from 0 m/s to 15 m/s and remains at 15 m/s, the resulting equilibrium diff-Δ will reach a maximum of 1.8% after 6 days based on the estimated effect of bubbles injected into the surface ocean and the solubility differences between N_2 and Ar. The expected change in gas saturation and gas ratio saturation from temperature change and enhanced wind are indicated in Figures 1 and 2 where the relaxation back to equilibrium following a high wind event is slow, and the water mass retains the gas signature from bubble injection and exchange for much longer.

3.2 Influence of sea ice on gas ratios

Another physical factor influencing gas saturation is sea ice formation or melt. Brine rejected from the ice matrix during ice formation is expected to be enriched in Ar, O_2, and N_2 due to the exclusion of larger gas molecules during the freezing process. This brine sinks to depth when formed at the ice-water interface, enriching deep water in these gases. When vertical mixing of these deep waters occurs, a brine signal may be observed in the resulting water, which is expected to be enriched in Ar compared to N_2 based on gas partitioning between bubbles, ice, brine, and residual water (Hamme 2003). This brine signal is expected to have lower O_2/Ar than O_2/N_2 due to the gas rejection signature when sea ice is formed, while modification of this brine may occur while within the sea ice matrix (via photosynthesis and respiration, Zhou et al. 2014) and within rejected brine once at depth (respiration). In contrast, the meltwater signal is expected

to be depleted in larger gases (Ar, O_2, N_2) due to gas exclusion during sea ice formation. Low concentrations of Ar and N_2 are expected upon ice melt due to this gas exclusion, while potential for within- and under-ice production may elevate O_2. In contrast, the entrapment of bubbles under the impermeable ice layer may result in supersaturation of these gases during the top layer of ice melt (Zhou et al. 2014), depending on the dynamics of melting. Any meltwater signals imparted into the surface layer will be short-lived due to air-sea equilibration upon melting. This meltwater effect is not anticipated to be represented in this dataset due to lack of sea ice during this cruise, but brine signatures could be observed in areas where vertical mixing brings waters that have been seasonally isolated at depth to the surface.

3.3 Biological influences on dissolved N_2

Biological influences on dissolved N_2 in the ocean are typically small, but should be assessed in regions known to be influenced by biological processes that consume and produce N_2 via dinitrogen fixation and denitrification, respectively. The effect of nitrogen fixation relative to N_2, calculated based on the maximum rate of nitrogen fixation estimated by Shiozaki (2018) in the Chukchi Sea over two weeks results in a decrease in dissolved nitrogen gas of less than 0.01%, an amount that has no effect on the estimates of $\Delta O_2/N_2$ here. In contrast, the effect of denitrification on the shallow Bering and Chukchi shelves has a potentially greater effect on N_2, as is considered here. With denitrification occurring at depth, bottom waters are expected to be enhanced in dissolved N_2 to varying degrees. Vertical mixing of deep water containing

biologically-elevated dissolved N_2 will influence the O_2/N_2 ratios measured at the surface, resulting in lower than expected $\Delta O_2/N_2$.

We can estimate the potential impact of these processes for our study region using estimated upper bounds for the amount of denitrification and annamox occurring at depth in the Bering and Chukchi Seas. Based on seasonal dissolved inorganic nutrient deficits of 3.9 µM N at depth on the Chukchi shelf (Mordy et al. in review), if we assume complete vertical mixing of the water column when the mixed layer makes up the upper 40% of the water column (e.g. 20 m mixed layer in 50 m water column), a 0.32% decrease in $\Delta O_2/N_2$ would occur. The above estimates of the effect of denitrification on $\Delta O_2/N_2$ are based on complete vertical mixing of the water column and assume the total observed nitrogen deficit was produced through denitrification/annamox processes resulting in N_2 gas production, and as such, these represent an upper limit to the potential impact of denitrification. Since the Chukchi Sea is seasonally well-stratified, this type of complete water column mixing is only likely to occur near coastal features or areas with enhanced mixing, such as near Bering Strait. In scenarios with significant vertical mixing, the use of $\Delta O_2/N_2$ as a tracer of net biological oxygen production is not advised due to the non-steady state nature of the mixed layer, and these areas can be identified and excluded from analysis by observing water mass properties typical of bottom water in this region (e.g. low O_2, negative net biological oxygen production, elevated salinity). A more realistic scenario involving vertical mixing of a small fraction (20%) of the water column (based on average nitrogen deficits stated above) would result in a 0.06% decrease in $\Delta O_2/N_2$, a small and likely indiscernible bias of the measurement.

3.4 Spatial Patterns

A comparison of spatial distributions of ΔO_2 with $\Delta O_2/Ar$ for OS1901 illustrates how oxygen supersaturation and net biological oxygen supersaturation are related (Figure 3). Note that there are regions with strong oxygen supersaturation that are co-located with negative $\Delta O_2/Ar$, suggesting that oxygen supersaturation was purely driven by physical factors (e.g. wind and bubbles or warming), with the biological signal opposing this trend (but not completely compensating for physical effects). Other areas have positive $\Delta O_2/Ar$ and more positive ΔO_2, suggesting a mix of physical and biological forcing of oxygen supersaturation. The spatial patterns in $\Delta O_2/Ar$ indicate areas of large net biological supersaturation with $\Delta O_2/Ar$ peaks

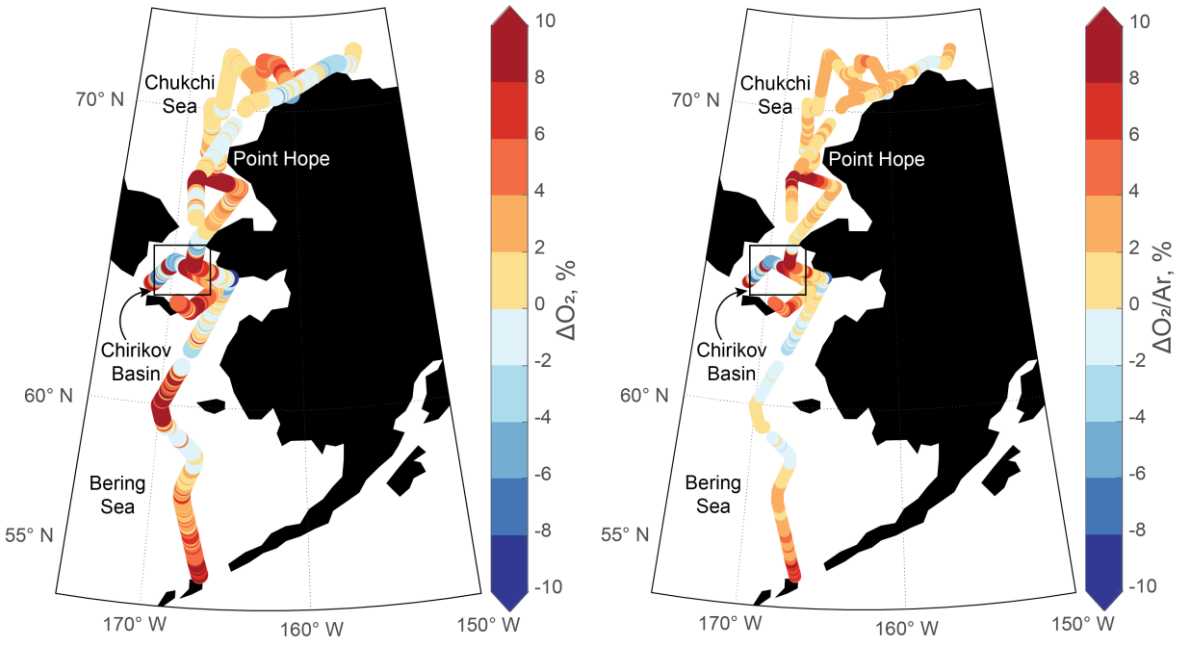

Figure 3: ΔO_2 and $\Delta O_2/Ar$ along the cruise track (scale attenuated to make near-equilibrium trends more visible). These trends in $\Delta O_2/Ar$ are also seen in $\Delta O_2/N_2$ (not shown here), while more noise is present in that signal.

above 30% near the Aleutian arc, in Chirikov Basin and off of Point Hope. Both Chirikov Basin and Point Hope are established biological hotspots (Grebmeier et al. 2015).

In these biological hotspots, chlorophyll-a based on underway fluorescence from a Seabird ECO-FL fluorometer was elevated in all but one occurrence (Figure 4). The region off of Point Hope was occupied twice (on 8/11 and 8/23), where low concentrations of chlorophyll-a were observed during the first occupation, followed by a peak in chlorophyll-a with the later occupation. A mismatch between chlorophyll-a and O_2/Ar is expected at times because of the different timescales associated with dissolved O_2 and biomass turnover in the surface ocean (2-3 weeks vs. days). Chlorophyll-a data from MODIS-A (NASA Goddard Space Flight Group; Ocean Ecology Laboratory; Ocean Biology Processing Group, https://modis.gsfc.nasa.gov/data/) were sparse in the weeks prior to shipboard measurements, but the edge of a bloom with elevated

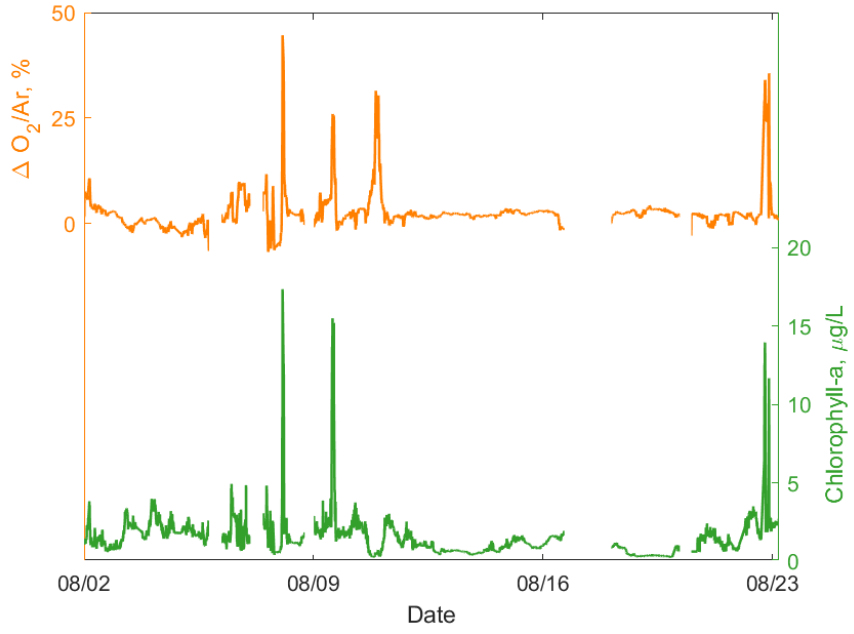

Figure 4: Underway measurements of ΔO_2/Ar and chlorophyll-a based on underway fluorescence throughout the cruise.

chlorophyll-a was seen off of Point Hope on August 4, 2019, about 7 days prior to shipboard measurements in the same location. This elevated biological production was indicated in the shipboard O_2/Ar, while the production biomass would have attenuated over a shorter timescale, resulting in low underway fluorescence.

In the middle section of the Bering Sea, ΔO_2 is generally positive and ΔO_2/Ar is generally negative, consistent with physical supersaturation of oxygen in the surface ocean due to both cooling water and increased wind speed ($\Delta O_2 > 0$) and net heterotrophic biological activity (ΔO_2/Ar <0). In Chirikov Basin, ΔO_2/Ar was variable, with patches of large supersaturation as well as undersaturation that could be attributed to the dynamic nature of water masses mixing in this area (Danielson et al. 2017). The areas with both negative and positive ΔO_2/Ar in the western part of Bering Strait are in significantly colder, saltier, nitrate-rich water (salinity >32.5, NO_3>20 µM from an underway In Situ Ultraviolet Spectrophotometer (ISUS) nutrient sensor, data not shown) typical of Anadyr water (Grebmeier et al. 2006). The ΔO_2/Ar signals here likely reflect a combination of recent vertical mixing (bringing subsurface water with a depleted O_2 signature to the surface) and patchy production sparked by high nutrient Anadyr water when light and stratification conditions were favorable. In the majority of the Chukchi Sea, excluding biological hotspots with ΔO_2/Ar > 5%, net biological oxygen supersaturation was positive, indicating net autotrophy (ΔO_2/Ar=2 ± 1%).

3.5 EIMS-GTD Comparison

Comparison of $\Delta O_2/N_2$ and $\Delta O_2/Ar$ for OS1901 indicates close agreement, where both ratios indicate net supersaturation of oxygen for the majority of the cruise (Figure 5). In areas of large biological oxygen supersaturation, the ratios are observed to differ, where $\Delta O_2/N_2$ is consistently larger than $\Delta O_2/Ar$ (Figure 5A). The memory effects associated with the EIMS effectively slow down the $\Delta O_2/Ar$ measurements, resulting in $\Delta O_2/Ar$ that don't reach the true maximum value during sharp gradients, while $\Delta O_2/N_2$ is thought to be capturing these maxima more accurately due to the faster response time. This difference in ratios in regions with large gradients is lessened by the exponentially filtered $\Delta O_2/N_2$ ratio, although this filter does not fully approximate the data smearing effects of the EIMS equilibrator. Large gradients may mask differences simply because of the mathematical differences of the filters applied to each method. This exponentially filtered data is only used when calculating diff-Δ, while noise-filtered $\Delta O_2/N_2$ is shown in all other plots.

By comparing $\Delta O_2/N_2$ and $\Delta O_2/Ar$ values with diff-Δ, biases of individual methods can be assessed. The mean and median of diff-Δ over the cruise was 0.56% and 0.51%, while there were many large excursions from these values (Figure 5B). In particular, deviations in diff-Δ occurred during time periods where strong gradients in oxygen were encountered and in areas with overwhelming bubble influence (shaded regions, Figure 5A). One way of assessing causes of these excursions in diff-Δ is by comparing diff-Δ values to an approximation of physical forcing, estimated as:

$$\Delta O_2^{phys} = \Delta O_2^{total} - \Delta O_2/Ar \quad (11)$$

where the last term represents ΔO_2^{bio} (Shadwick et al. 2015). When ΔO_2^{phys} is positive, a positive physical supersaturation of oxygen is estimated and could be indicative of recent warming of the water mass or potential influence of bubbles. Along the same lines, a negative value is expected when biological oxygen saturation is greater than total oxygen saturation, potentially caused by recent cooling. This estimate of ΔO_2^{phys} has a mean value of 4.65% (Figure 5B).

We also calculated ΔN_2 as a tracer that is particularly sensitive to bubble-driven physical gas supersaturation Due to the low solubility of N_2 combined with the high abundance of N_2 in the atmosphere, nitrogen is sensitive to bubble injection and exchange. Therefore, nitrogen supersaturation (ΔN_2) roughly approximates the degree of bubble-driven physical gas supersaturation. This was calculated and residual filtered to remove outliers and noise, with a

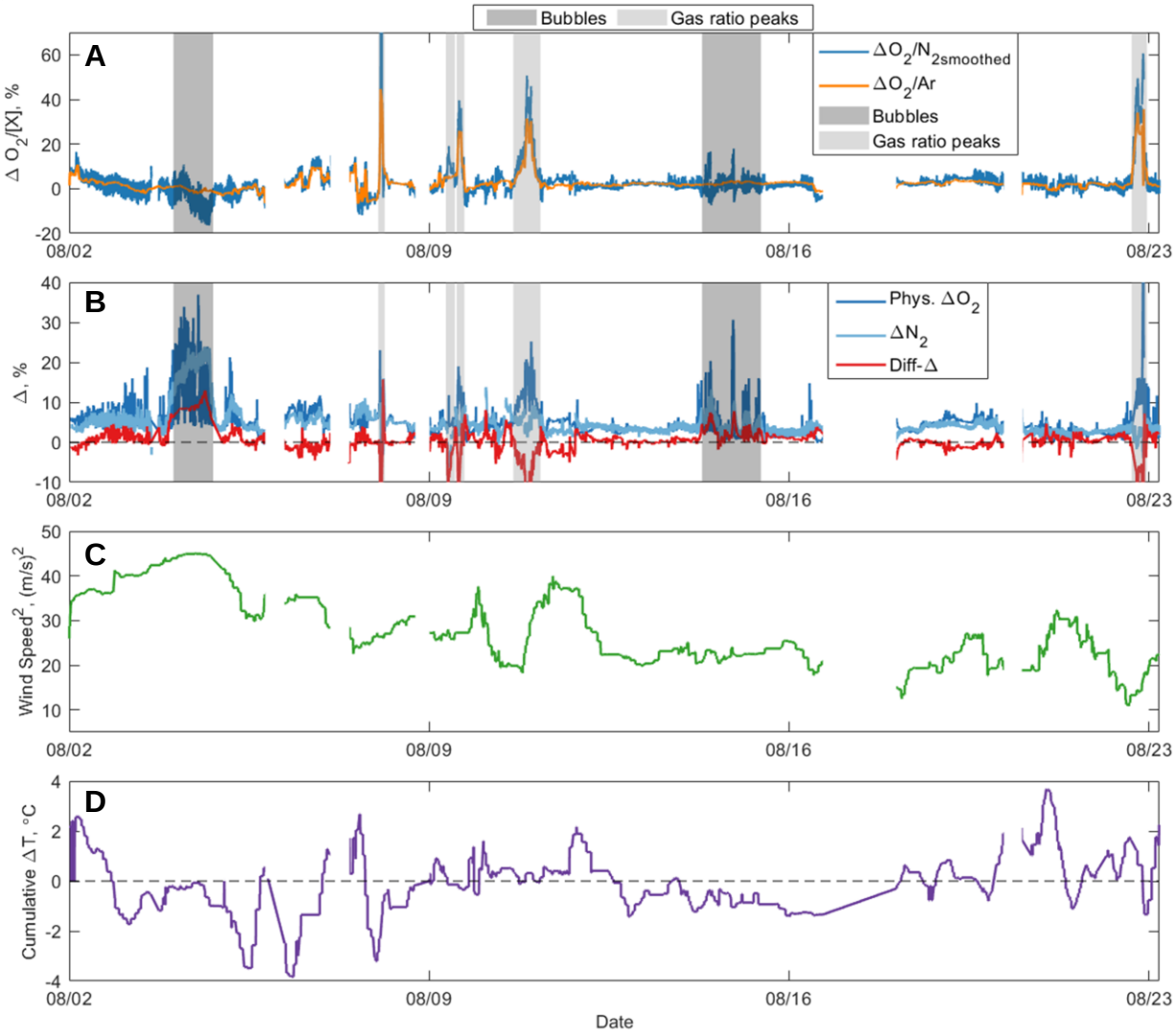

Figure 5: (A) Time-series of $\Delta O_2/Ar$ and smoothed $\Delta O_2/N_2$, where shaded areas indicate either noise due to bubbles in the underway seawater line or large gradients in gas ratios as determined by observation. The $\Delta O_2/N_2$ peak off the chart is at 127%. (B) Time-series of Diff-Δ, ΔO_2-physical, and smoothed ΔN_2, where artifacts of the data due to mismatched gas ratio peaks (shaded in light gray) are off the chart and should not be considered (C) Average squared wind speed over the two weeks prior to sampling. (D) Cumulative temperature change over two weeks prior to sampling based on satellite SST reanalysis.

mean value of 4.3%. The similarity between average ΔO_2^{phys} and that attributed to bubbles (Figure 5B) suggests that bubble injection and exchange is driving much of the physical oxygen supersaturation, while warming (cooling) could also increase (decrease) the total physical

oxygen supersaturation. The overwhelmingly positive ΔO_2^{phys} is amplified in areas with bubble noise, an observation substantiated by the coinciding ΔN_2 peaks, while the cumulative effect of previous bubble driven N_2 supersaturation is likely present in areas without observed bubbles as well.

To reach a bubble-driven N_2 supersaturation of 4%, similar to the estimated average for this cruise, wind speed would need to be greater than 15 m s^{-1} for a short period of time, although average daily wind speeds over the two previous weeks were below 6.5 m s^{-1} based on NCEP Reanalysis data. However, the daily average wind speeds from NCEP Reanalysis may be biased low in this region; we assessed this by comparing a subset of the reanalysis wind speed data to wind speed at the Barrow, AK NOAA CMDL meteorological station. When the ship occupied the area surrounding Pt. Barrow, AK, the average wind speed over two weeks prior to occupation as determined by NARR wind speed was often lower than the wind speed measured at Barrow, with an average difference of 0.15 m s^{-1}. Additionally, due to the quick response of dissolved gas saturation to an increase in wind speed (Figure 2B), short periods with high winds will have a disproportionately large effect on gas supersaturation that may not be evident in the average wind speed.

Further, a portion of the ΔO_2^{phys} estimated here could have been caused by recent warming of the water mass. The cumulative temperature change over the preceding two weeks shows intermittent cooling and warming (Figure 5D) that does not strongly support the hypothesis that warming was the primary driver of oxygen supersaturation. However, the cumulative

temperature change presented here is based on a fixed geo-referenced grid and does not take into account the dynamic nature of water mass movement. For example, if a recently warmed water parcel horizontally advected into an area on the cruise track, the cumulative temperature change calculated based on satellite SST for a fixed location will not accurately capture the warming.

We attribute the few regions with large estimated physical oxygen supersaturation that align with peaks in the gas ratio-derived biological oxygen supersaturation and negative excursions in diff-Δ to be artifacts of the minute-timescale instrument sensitivities (Figure 5). Since the calculation of both diff-Δ and ΔO_2^{phys} depend on $\Delta O_2/Ar$, discrepancies in $\Delta O_2/Ar$ will cause diff-Δ and ΔO_2^{phys} to inversely covary during strong gradients in oxygen when measured $\Delta O_2/Ar$ may be lower than the true value due to equilibrator memory effects. Therefore, these inversely correlated peaks are determined to be primarily artifacts of the data based on the co-dependence on $\Delta O_2/Ar$ that was established to have a dampened signal during peaks in oxygen due to EIMS membrane memory effects.

Due to the large range of diff-Δ along this cruise track, regions with significant bubble noise and those with steep oxygen

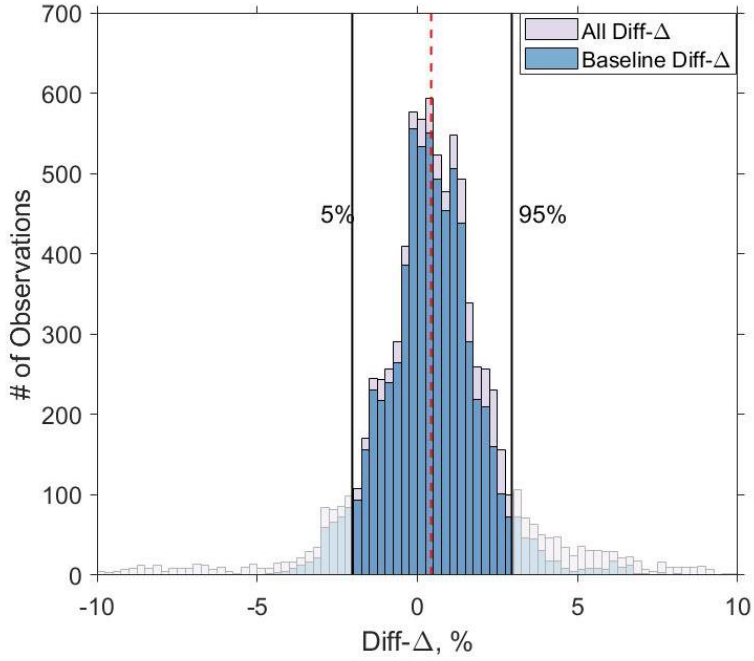

Figure 6: Histogram of diff-Δ observations with all values and when skewed data due to bubbles and steep gas peaks are excluded.

gradients skew the data distribution. This skewed data due to bubbles and steep gas peaks is observed in Figure 6. When these large deviations are excluded in the “normal” diff-Δ, as visually determined by high frequency noise or steep gradients, the bulk offsets in gas ratios are more clearly discerned, where the mean and median of diff-Δ is 0.46% and 0.43%. The distribution of diff-Δ is roughly normal, where 90% of observations fall between -2.03% and 2.95%.

A potential source of bias in $\Delta O_2/N_2$ and thus diff-Δ may arise from the assumed saturation of less prevalent gases, particularly Ar. On this cruise, Ar concentrations were determined by EIMS O_2/Ar ratio and optode oxygen measurements (where $[Ar]=[O_2]_{optode}/[O_2/Ar]_{EIMS}$), yet these values were not used in calculations of $\Delta O_2/N_2$, as this study is intended to simulate the comparability of these methods and the inclusion of calculated Ar values are not anticipated to be available with most GTD deployments. If these calculated values for Ar were included, which indicate Ar was consistently supersaturated throughout this cruise, the bias in diff-Δ decreases to a mean and median of 0.30% and 0.28%. Overall, based on the average wind speed of 5 m/s over the course of the cruise, we expect an average diff-Δ of 0.21% based on the bubble-driven gas supersaturation. Therefore, about half of the bias in diff-Δ is attributed to bubble-driven differences in gas saturation (0.21%), while another 0.16% can be attributed to assumptions made about Ar saturation. The remaining bias in diff-Δ of about 0.1% could be due to some combination of temperature-driven deviations and variations from the mean wind speed.

This comparison of methods revealed a smoothing of sharp oxygen gradients in the EIMS data, which we attribute to the EIMS equilibrator memory effect. Optode O_2 peaks were much sharper and reached higher maximum values in areas with large gradients; in these areas, which were also regions with elevated net biological oxygen production, the observed $\Delta O_2/N_2$ was up to 1.5 times greater than $\Delta O_2/Ar$. The difference in these ratios during steep gradients revealed this EIMS memory effect, indicating these $\Delta O_2/Ar$ measurements were not capturing the true value of high productivity signals. Therefore, in regions with sharp gradients and localized productivity peaks, such as those encountered in this study in the Chirikov basin and the vicinity of Pt. Hope, GTD measurements may more accurately capture absolute productivity values, while EIMS-based observations are critical for accuracy in oligotrophic, lower-productivity regions that characterized the rest of the cruise track. On future deployments, EIMS equilibrator response times could also be better optimized by using an equilibrator cartridge with a smaller headspace to water volume ratio, while including a recirculating desiccant loop for constant removal of water vapor in the equilibrator has also been shown to improve response time (Manning et al. 2016).

3.6 Net Community Production

The median NCP estimated by O_2/Ar and O_2/N_2 was 7.49 ± 2.34 and 7.16 ± 2.68 mmol O_2 m^{-2} day^{-1}, respectively, for all regions with comparable data (which excludes bubble-impacted areas, as well as one region in Chirikov Basin with a clear vertical mixing signal). The overall NCP estimated by O_2/Ar and O_2/N_2 are similar, while differences include the discrepancy in maximum NCP in regions with large gradients as previously discussed, as well as increased noise in O_2/N_2 signal (Figure 7).

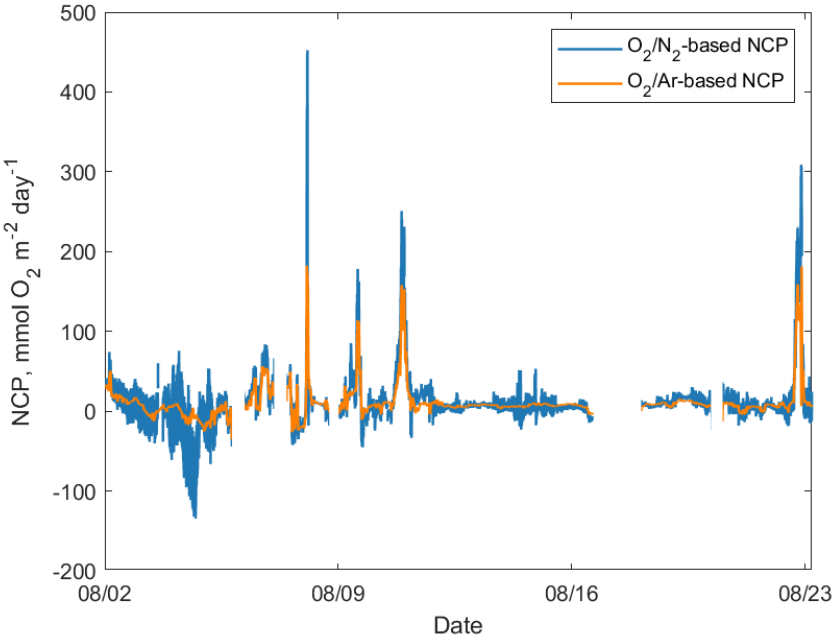

Figure 7: NCP calculated based on O_2/Ar and residual filtered O_2/N_2 for measurements within the bounds described.

The median NCP based on O_2/Ar measurements was 7.63 mmol O_2 m^{-2} day^{-1}, while 95% of the values fell between -5.1 and 51.9 mmol O_2 m^{-2} day^{-1}. Assuming an O_2:C ratio of 1.4 for new production based primarily on nitrate (Laws 1991), O_2/Ar-based NCP ranged from below zero to >1000 mg C m^{-2} day^{-1}, with a median of 67 mg C m^{-2} day^{-1} during this August cruise. Since this measurement technique integrates over the preceding weeks, this provides a unique dataset

that may be more representative of the NCP in a region. Other measurements from this region integrate over different timescales (Table 1), which makes comparison challenging.

Table 1: NCP comparisons in Chukchi Sea

Method	NCP (mg C m^{-2} day^{-1})	Region	Timescale	Source
DIC Drawdown	8 to >2000	Northeast Chukchi Sea	Seasonal, spring to summer	Mathis et al. 2009
Nutrient drawdown	1167	Southern Chukchi Sea	60-day growing period	Codispoti et al. 2013
Seasonal nitrate	82 to 192	Eastern Chukchi Sea	Annual, from seasonal nitrate between 2010-2018	Mordy et al. 2020
Shipboard O_2/Ar	8 to 86 [1 to 10 mmol O_2 m^{-2} day^{-1}]	Chukchi Sea	Integrated over few weeks in October 2011 and 2012	Juranek et al. 2019
Shipboard O_2/Ar	0 to >1000	Chukchi Sea	Integrated over few weeks in August 2019	this study

Seasonal estimates based on DIC and nutrient drawdown (Mathis et al. 2009; Codispoti et al. 2013) include the spring bloom, and are therefore expected to be considerably higher than the rates measured in August, post-bloom, while annual measurements (Mordy et al. 2020) include the dark, ice-covered winter when production is absent. In summary, the NCP values from this dataset are in line with others in the Chukchi Sea which do not include the spring bloom production. With the spatially resolved data from this cruise, local hotspots can be assessed, while drivers of biological production can also be evaluated. Areas of high net biological productivity from this cruise were consistent with biological hotspots in the Chirikov Basin and off of Point Hope, which are regularly observed as part of the Distributed Biological Observatory (DBO 2 and 3, respectively, Grebmeier et al. 2010). This data supports previous high resolution measurements that suggest production is patchy and sparse (Juranek et al. 2019), patterns that

may not be incorporated into remote sensing approaches that compile data from clear viewing days where overall trends in productivity may be misrepresented.

3.7 Uncertainty Analysis

To estimate uncertainty in EIMS- and GTD-based NCP, we used a Monte Carlo approach that involves randomly varying the estimated error of each parameter involved in calculating NCP, assuming a normal distribution of error. The values used in these determinations are found in Table 1, where uncertainty was calculated based on 1000 determinations of $\Delta O_2/Ar$- and $\Delta O_2/N_2$-based NCP with Equation 10 for gas ratios observed on this cruise. Uncertainty in the gas transfer coefficient, k_{O2} (± 20%) (Wanninkhof 2014), makes up the largest component of uncertainty in NCP. The resulting uncertainty for a simulated NCP of 10 mmol O_2 per m^2-day from O_2/Ar and O_2/N_2 is 22% and 38%, respectively, which decreases with larger NCP. The uncertainty in O_2/Ar-based NCP ranged from 16% to >100%, while the uncertainty for O_2/N_2-based NCP ranged from 23% to >100%. While uncertainty in $\Delta O_2/N_2$ becomes large in areas where net biological oxygen supersaturation nears zero, these estimates still discern the relative magnitude and direction of NCP for the majority of observations on this cruise, so long as the oxygen measurements used to compute O_2/N_2 are well-calibrated.

Relative uncertainty in both $\Delta O_2/Ar$ and $\Delta O_2/N_2$ increases as the ratios approach equilibrium, resulting in large uncertainty for near-equilibrium gas ratios, while uncertainty becomes less significant as gas saturation ratios deviate from equilibrium. Absolute uncertainty in the measurement of $\Delta O_2/Ar$ of ± 0.25% was determined by the standard deviation of O_2/Ar in air standards (n=27) measured by IRMS, since EIMS O_2/Ar measurements were corrected to the calibration bottle samples analyzed by IRMS. For GTD-based measurements, an absolute precision in the measurement and calculation of $\Delta O_2/N_2$ of ±0.57% was determined by propagation of error in Equations 6 and 7. The corresponding uncertainties in the measured values also vary depending on how far $\Delta O_2/Ar$ and $\Delta O_2/N_2$ are from equilibrium, as indicated in Table 1.

Table 2: Error estimates used in Monte Carlo approach of uncertainty and output uncertainty in $\Delta O_2/Ar$ and $\Delta O_2/N_2$

Source	**Estimated Error**		
O_2/Ar_{meas}	0.25% (st. dev. of O_2/Ar in air)		
O_{2sol}	0.3% (Garcia And Gordon 1992)		
Gas exchange, k	20% (Wanninkhof 2014)		
GTD total pressure	0.2% or 2 mbar (Pro-Oceanus TDGP manual)		
O_2 (Winkler-corrected optode)	0.5% or 1.1 mbar (McNeil et al. 2005)		
Atmospheric pressure (NCEP reanalysis)	0.5% or 5 mbar (Padin et al. 2007)		
Uncertainty			
	Absolute	Relative	
		$\Delta O_2/[X] = 1\%$	$\Delta O_2/[X] = 10\%$
$\Delta O_2/Ar$	0.25%	24.2%	2.5%
$\Delta O_2/N_2$	0.57%	58.4%	6.2%

The uncertainty outlined above is based on the accuracy in the measurement and calculation of $\Delta O_2/N_2$, and does not include potential biases from physical forcing that cause this tracer to inaccurately track ΔO_{2bio}. The physically forced biases impacting

$\Delta O_2/N_2$ represent another type of uncertainty that is not quantifiable without paired methods as conducted here. These physical biases can be assessed using remote sensing data over the weeks preceding measurements, although water mass movement can create challenges in remote sensing data interpretation. Based on the median diff-Δ of 0.51% for all measurements and 0.43% for "normal" measurements, $\Delta O_2/N_2$ is consistently biased low with respect to $\Delta O_2/Ar$ measurements. Based on the average wind speed, we expect $\Delta O_2/N_2$ to be 0.21% lower than $\Delta O_2/Ar$ based solely on the bubble-driven gas supersaturation at equilibrium, which is a lower limit to this value due to the squared dependence of bubble effects on wind speed where average wind speed doesn't fully account for short periods of high wind. Therefore, the remaining difference in these gas ratios of about 0.22% for "normal" measurements is attributed to temperature-driven deviations, as well as variations in the degree of bubble processes.

When the GTD/optode technique is used as a standalone method, remote sensing data could potentially be assessed to determine the expected physical contribution to bias in this method. In this dataset, changes in wind speed and SST from remote data are presented in comparison to diff-Δ (Figure 5) due to the expected association between diff-Δ and physical forcing of gases. The expected effect of bubble injection is to increase diff-Δ whereas warming (cooling) is expected to decrease (increase) diff-Δ, respectively. There is no clear association between the physical forcing parameters presented here. This is confirmed by linear regression analysis of diff-Δ and average wind speed or temperature change that both indicate no significant correlation (not shown). While the direct correlation between remote sensing parameters and diff-Δ was not significant for this cruise, the wind speed data from the weeks preceding shipboard observations

can be used to estimate the bias in diff-Δ due to bubble processes, as is done here with an average bias of 0.2% over the cruise. This technique could be employed within regions of the cruise track as well to get a better sense of the bubble influence in each area. Overall, the drivers of productivity

Better understanding of marine productivity patterns and how they relate to other hydrographic features could help to decipher the dynamic environmental factors driving this production. In addition, climate change impacts the functioning of the biological pump, where warming waters may accelerate recycling of organic matter in the surface ocean, thus decreasing export efficiency, resulting in slower biologically driven uptake of CO_2 from the atmosphere. This resembles a positive feedback loop where higher atmospheric CO_2 then enhances warming further. A shift in the production regime in this region would also impact the ecosystem community composition, which may shift from a primarily benthic community on shallow shelves such as the Chukchi towards a pelagic community.

3.8 Strengths and Weaknesses of GTD and EIMS approaches

A potential limitation of gas ratio estimates from a GTD is the dependence on accurate oxygen measurements when calculating O_2/N_2. This requires optode calibration to adjust for offsets and drift, where a 5% offset in the optode O_2 (the average offset on this cruise), results in a difference of 6.5% in O_2/N_2. Without reliable oxygen calibrations, this scale of difference could result in ambiguous NCP estimates derived from O_2/N_2, although areas with strong biological signals are

still qualitatively identified despite this potential uncertainty. This is expected to be a greater issue when frequent O_2 calibration samples are not feasible, e.g. with autonomous deployments, although periodic air calibration of deployed optodes could serve as an alternative calibration method (Bittig and Körtzinger 2015; Bushinsky et al. 2016).

Another challenge experienced with the GTD-optode system on this cruise was the effect of bubbles. Bubble effects are likely to be a problem for ships with shallow seawater intakes (<5 m) operating in moderate to rough sea states. While a debubbling chamber could be employed to limit this noise, areas with extensive bubble influence in the GTD/optode data are expected to be influenced by bubble injection and exchange in the water column as well, which would still bias the measured O_2/N_2.

4 Conclusions

This cruise provided a range of conditions under which to assess the efficacy of the GTD/optode system compared to the EIMS for estimating net biological oxygen production. The takeaways from this method comparison include the relatively quick response time of the GTD, which is not subject to memory effects, allowing for sharp gradients in gas saturation to be well characterized. This method is subject to greater biases from physical forcing, including warming, bubble injection, and meltwater input, although the only direct relation observed between physical effects and diff-Δ was with bubbles. With further comparisons of $\Delta O_2/N_2$ to established methods of measuring net biological oxygen production, observation of the physical factors that cause

$\Delta O_2/N_2$ to diverge from established methods ($\Delta O_2/Ar$) could be understood enough to potentially correct for these offsets with additional physical data (e.g. time series measurements of temperature and salinity on a mooring or drifter that may observe temperature change in a given water mass). The utility of this method depends on the productivity in an area: the GTD/optode system is expected to capture large signals in net biological oxygen supersaturation, while oligotrophic areas with low net productivity may be difficult to determine with certainty since $\Delta O_2/N_2$ will be near zero and the biological oxygen supersaturation may be overwhelmed by the physical factors influencing gas solubility. The dependence of $\Delta O_2/N_2$ on calibrated oxygen measurements needs to be considered when using the GTD/optode method in an autonomous deployment. By incorporating periodic air measurements by the optode, a strategy that has previously been used on floats, reliable oxygen measurements could be maintained throughout a GTD/optode deployment, providing a reference for calibration.

NCP over the course of this cruise was patchy, with localized areas of high NCP associated with known biological hotspots for short time periods. This was captured in the NCP measured by both ΔO2/Ar and ΔO2/N2 due to the integration timescale (2-3 weeks), while other methods would have missed some of this production either due to the instantaneous nature of measurements (bottle incubations, chlorophyll measurements) or due to cloud cover limiting remote sensing data. Therefore, these gas tracer techniques provide unique measurements that are more comprehensive than discrete measurement, capturing sparse and short-lived blooms better than other methods.

5 Acknowledgements

We thank Sarah Donohoe for her analysis of oxygen samples at sea. We also thank the captain and crew of R/V *Ocean Starr* for their shipboard support. This cruise was part of the Arctic Integrated Ecosystem Survey (Arctic IES), funded as part of the North Pacific Research Board's (NPRB's) Arctic Integrated Ecosystem Research Program (IERP). This work was supported by NSF awards 1928684 and 1949593 to LWJ.

6 References

Andersen, J. K., L. M. Andreassen, E. H. Baker, and others. 2020. State of the Climate in 2019: The Arctic J. Richter-Menge and M.L. Druckenmiller [eds.]. Bull. Am. Meteorol. Soc. **101**: S239–S286. doi:10.1175/BAMS-D-20-0086.1

Anderson, L. G., and S. Kaltin. 2001. Carbon fluxes in the Arctic Ocean—potential impact by climate change. Polar Res. **20**: 225–232. doi:10.3402/polar.v20i2.6521

Arrigo, K. R., and G. L. van Dijken. 2015. Continued increases in Arctic Ocean primary production. Prog. Oceanogr. **136**: 60–70. doi:10.1016/j.pocean.2015.05.002

Arrigo, K. R., G. van Dijken, and S. Pabi. 2008. Impact of a shrinking Arctic ice cover on marine primary production. Geophys. Res. Lett. **35**: 1–6. doi:10.1029/2008GL035028

Bélanger, S., M. Babin, and J.-É. Tremblay. 2013. Increasing cloudiness in Arctic damps the increase in phytoplankton primary production due to sea ice receding. Biogeosciences **10**: 4087–4101. doi:10.5194/bg-10-4087-2013

Benson, B. B., and D. Krause. 1984. The concentration and isotopic fractionation of oxygen dissolved in freshwater and seawater in equilibrium with the atmosphere1. Limnol. Oceanogr. **29**: 620–632. doi:10.4319/lo.1984.29.3.0620

Bittig, H. C., and A. Körtzinger. 2015. Tackling oxygen optode drift: Near-surface and in-air oxygen optode measurements on a float provide an accurate in situ reference. J. Atmos. Ocean. Technol. **32**: 1536–1543. doi:10.1175/JTECH-D-14-00162.1

Bushinsky, S. M., S. R. Emerson, S. C. Riser, and D. D. Swift. 2016. Accurate oxygen measurements on modified argo floats using in situ air calibrations. Limnol. Oceanogr. Methods **14**: 491–505. doi:10.1002/lom3.10107

Carmack, E. C., and P. Wassmann. 2006. Food webs and physical–biological coupling on pan-Arctic shelves: Unifying concepts and comprehensive perspectives. Prog. Oceanogr. **71**: 446–477. doi:10.1016/j.pocean.2006.10.004

Carmack, E., I. Polyakov, L. Padman, and others. 2015. Toward quantifying the increasing role of oceanic heat in sea ice loss in the new arctic. Bull. Am. Meteorol. Soc. **96**: 2079–2105. doi:10.1175/BAMS-D-13-00177.1

Carpenter, J. H. 1965. The Accuracy of the Winkler Method for Dissolved Oxygen Analysis. Limnol. Oceanogr. **10**: 135–140. doi:10.4319/lo.1965.10.1.0135

Cassar, N., B. A. Barnett, M. L. Bender, J. Kaiser, R. C. Hamme, and B. Tilbrook. 2009. Continuous High-Frequency Dissolved O 2 /Ar Measurements by Equilibrator Inlet Mass Spectrometry. Anal. Chem. **81**: 1855–1864. doi:10.1021/ac802300u

Codispoti, L. A., V. Kelly, A. Thessen, P. Matrai, S. Suttles, V. Hill, M. Steele, and B. Light. 2013. Synthesis of primary production in the Arctic Ocean: III. Nitrate and phosphate based estimates of net community production. Prog. Oceanogr. **110**: 126–150. doi:10.1016/j.pocean.2012.11.006

Craig, H., and T. Hayward. 1987. Oxygen Supersaturation in the Ocean: Biological Versus

Physical Contributions. Science (80-.). **235**: 199–202. doi:10.1126/science.235.4785.199

Danielson, S. L., L. Eisner, C. Ladd, C. Mordy, L. Sousa, and T. J. Weingartner. 2017. A comparison between late summer 2012 and 2013 water masses, macronutrients, and phytoplankton standing crops in the northern Bering and Chukchi Seas. Deep. Res. Part II Top. Stud. Oceanogr. **135**: 7–26. doi:10.1016/j.dsr2.2016.05.024

DeGrandpre, M., W. Evans, M. L. Timmermans, R. Krishfield, B. Williams, and M. Steele. 2020. Changes in the Arctic Ocean Carbon Cycle With Diminishing Ice Cover. Geophys. Res. Lett. **47**. doi:10.1029/2020GL088051

Ducklow, H., and S. C. Doney. 2013. What is the metabolic state of the oligotrophic ocean? a debate. Ann. Rev. Mar. Sci. **5**: 525–533. doi:10.1146/annurev-marine-121211-172331

Emerson, S. R., C. Stump, B. Johnson, and D. M. Karl. 2002. In situ determination of oxygen and nitrogen dynamics in the upper ocean. Deep Sea Res. Part I Oceanogr. Res. Pap. **49**: 941–952. doi:10.1016/S0967-0637(02)00004-3

Emerson, S. R., C. Stump, and D. Nicholson. 2008. Net biological oxygen production in the ocean: Remote in situ measurements of O 2 and N 2 in surface waters. Global Biogeochem. Cycles **22**: n/a-n/a. doi:10.1029/2007GB003095

Eppley, R. W., and B. J. Peterson. 1979. Particulate organic matter flux and planktonic new production in the deep ocean. Nature **282**: 677–680. doi:10.1038/282677a0

Eveleth, R., N. Cassar, R. M. Sherrell, H. Ducklow, M. P. Meredith, H. J. Venables, Y. Lin, and

Z. Li. 2017. Ice melt influence on summertime net community production along the Western Antarctic Peninsula. Deep. Res. Part II Top. Stud. Oceanogr. **139**: 89–102. doi:10.1016/j.dsr2.2016.07.016

Eveleth, R., M. L. Timmermans, and N. Cassar. 2014. Physical and biological controls on oxygen saturation variability in the upper Arctic Ocean. J. Geophys. Res. Ocean. **119**: 7420–7432. doi:10.1002/2014JC009816

Garcia, H. E., and L. I. Gordon. 1992. Oxygen solubility in seawater: Better fitting equations. Limnol. Oceanogr. **37**: 1307–1312. doi:10.4319/lo.1992.37.6.1307

Glueckauf, E. 1951. The Composition of Atmospheric Air, p. 3–10. *In* Compendium of Meteorology. American Meteorological Society.

Grebmeier, J. M., B. A. Bluhm, L. W. Cooper, and others. 2015. Ecosystem characteristics and processes facilitating persistent macrobenthic biomass hotspots and associated benthivory in the Pacific Arctic. Prog. Oceanogr. **136**: 92–114. doi:10.1016/j.pocean.2015.05.006

Grebmeier, J. M., L. W. Cooper, H. M. Feder, and B. I. Sirenko. 2006. Ecosystem dynamics of the Pacific-influenced Northern Bering and Chukchi Seas in the Amerasian Arctic. Prog. Oceanogr. **71**: 331–361. doi:10.1016/j.pocean.2006.10.001

Grebmeier, J. M., S. E. Moore, J. E. Overland, K. E. Frey, and R. Gradinger. 2010. Biological response to recent pacific arctic sea ice retreats. Eos (Washington. DC). **91**: 161–162. doi:10.1029/2010EO180001

Hamme, R. C. 2003. Applications of neon , nitrogen , argon and oxygen to physical , chemical and biological cycles in the ocean. 197.

Hamme, R. C., N. Cassar, V. P. Lance, and others. 2012. Dissolved O2/Ar and other methods reveal rapid changes in productivity during a Lagrangian experiment in the Southern Ocean. J. Geophys. Res. Ocean. **117**: 1–19. doi:10.1029/2011JC007046

Hamme, R. C., and S. R. Emerson. 2004. The solubility of neon, nitrogen and argon in distilled water and seawater. Deep. Res. Part I Oceanogr. Res. Pap. **51**: 1517–1528. doi:10.1016/j.dsr.2004.06.009

Hamme, R. C., and S. R. Emerson. 2006. Constraining bubble dynamics and mixing with dissolved gases: Implications for productivity measurements by oxygen mass balance. J. Mar. Res. **64**: 73–95. doi:10.1357/002224006776412322

Harada, N. 2016. Review: Potential catastrophic reduction of sea ice in the western Arctic Ocean: Its impact on biogeochemical cycles and marine ecosystems. Glob. Planet. Change **136**: 1–17. doi:10.1016/j.gloplacha.2015.11.005

Harding, K., K. A. Turk-Kubo, R. E. Sipler, M. M. Mills, D. A. Bronk, and J. P. Zehr. 2018. Symbiotic unicellular cyanobacteria fix nitrogen in the Arctic Ocean. Proc. Natl. Acad. Sci. U. S. A. **115**: 13371–13375. doi:10.1073/pnas.1813658115

Juranek, L. W., P. D. Quay, R. A. Feely, D. Lockwood, D. M. Karl, and M. J. Church. 2012. Biological production in the NE Pacific and its influence on air-sea CO 2 flux: Evidence

from dissolved oxygen isotopes and O 2 /Ar. J. Geophys. Res. Ocean. **117**. doi:10.1029/2011JC007450

Juranek, L. W., T. Takahashi, J. T. Mathis, and R. S. Pickart. 2019. Significant Biologically Mediated CO 2 Uptake in the Pacific Arctic During the Late Open Water Season. J. Geophys. Res. Ocean. **124**: 1–23. doi:10.1029/2018JC014568

Kaiser, J., M. K. Reuer, B. A. Barnett, and M. L. Bender. 2005. Marine productivity estimates from continuous O 2 /Ar ratio measurements by membrane inlet mass spectrometry. Geophys. Res. Lett. **32**. doi:10.1029/2005GL023459

Laws, E. A. 1991. Photosynthetic quotients, new production and net community production in the open ocean. Deep Sea Res. Part A. Oceanogr. Res. Pap. **38**: 143–167. doi:10.1016/0198-0149(91)90059-O

Lewis, K. M., G. L. Van Dijken, and K. R. Arrigo. 2020. Changes in phytoplankton concentration now drive increased Arctic Ocean primary production. Science (80-.). **369**: 198–202. doi:10.1126/science.aay8380

Lockwood, D., P. D. Quay, M. T. Kavanaugh, L. W. Juranek, and R. A. Feely. 2012. High-resolution estimates of net community production and air-sea CO 2 flux in the northeast Pacific. Global Biogeochem. Cycles **26**. doi:10.1029/2012GB004380

Manning, C. C., R. H. R. Stanley, and D. E. Lott. 2016. Continuous Measurements of Dissolved Ne, Ar, Kr, and Xe Ratios with a Field-Deployable Gas Equilibration Mass Spectrometer.

Anal. Chem. **88**: 3040–3048. doi:10.1021/acs.analchem.5b03102

Mathis, J. T., N. R. Bates, D. A. Hansell, and T. Babila. 2009. Net community production in the northeastern Chukchi Sea. Deep Sea Res. Part II Top. Stud. Oceanogr. **56**: 1213–1222. doi:10.1016/j.dsr2.2008.10.017

McNeil, C. L., D. Katz, R. Wanninkhof, and B. Johnson. 2005. Continuous shipboard sampling of gas tension, oxygen and nitrogen. Deep. Res. Part I Oceanogr. Res. Pap. **52**: 1767–1785. doi:10.1016/j.dsr.2005.04.003

Mesinger, F., G. DiMego, E. Kalnay, and others. 2006. North American Regional Reanalysis. Bull. Am. Meteorol. Soc. **87**: 343–360. doi:10.1175/BAMS-87-3-343

Mordy, C. W., S. Bell, E. D. Cokelet, and others. 2020. Seasonal and interannual variability of nitrate in the eastern Chukchi Sea: Transport and winter replenishment. Deep. Res. Part II Top. Stud. Oceanogr. **177**: 104807. doi:10.1016/j.dsr2.2020.104807

Mordy, C. W., L. Eisner, K. Kearney, and others. Spatiotemporal Variability of the Nitrogen Deficit on the Eastern Bering Sea Shelf. Rev.

NASA Goddard Space Flight Group; Ocean Ecology Laboratory; Ocean Biology Processing Group. Moderate-resolution Imaging Spectroradiometer (MODIS) Aqua Chlorophyll Data; 2018 Reprocessing. NASA OB.DAAC, Greenbelt, MD, USA. doi:data/10.5067/AQUA/MODIS/L3M/CHL/2018

Padin, X. A., M. Vázquez-Rodríguez, A. F. Rios, and F. F. Pérez. 2007. Atmospheric CO2

measurements and error analysis on seasonal air-sea CO2 fluxes in the Bay of Biscay. J. Mar. Syst. **66**: 285–296. doi:10.1016/j.jmarsys.2006.05.010

Quay, P., J. Stutsman, and T. Steinhoff. 2012. Primary production and carbon export rates across the subpolar N. Atlantic Ocean basin based on triple oxygen isotope and dissolved O 2 and Ar gas measurements. Global Biogeochem. Cycles **26**: 1–13. doi:10.1029/2010GB004003

Reuer, M. K., B. A. Barnett, M. L. Bender, P. G. Falkowski, and M. B. Hendricks. 2007. New estimates of Southern Ocean biological production rates from O2/Ar ratios and the triple isotope composition of O2. Deep Sea Res. Part I Oceanogr. Res. Pap. **54**: 951–974. doi:10.1016/j.dsr.2007.02.007

Semiletov, I., A. Makshtas, S.-I. Akasofu, and E. L Andreas. 2004. Atmospheric CO 2 balance: The role of Arctic sea ice. Geophys. Res. Lett. **31**: n/a-n/a. doi:10.1029/2003GL017996

Serreze, M. C., and J. Stroeve. 2015. Arctic sea ice trends, variability and implications for seasonal ice forecasting. Philos. Trans. R. Soc. A Math. Phys. Eng. Sci. **373**. doi:10.1098/rsta.2014.0159

Shadwick, E. H., B. Tilbrook, N. Cassar, T. W. Trull, and S. R. Rintoul. 2015. Summertime physical and biological controls on O2 and CO2 in the Australian Sector of the Southern Ocean. J. Mar. Syst. **147**: 21–28. doi:10.1016/j.jmarsys.2013.12.008

Shiozaki, T., A. Fujiwara, M. Ijichi, N. Harada, S. Nishino, S. Nishi, T. Nagata, and K. Hamasaki. 2018. Diazotroph community structure and the role of nitrogen fixation in the

nitrogen cycle in the Chukchi Sea (western Arctic Ocean). Limnol. Oceanogr. **63**: 2191–2205. doi:10.1002/lno.10933

Stammerjohn, S., R. Massom, D. Rind, and D. Martinson. 2012. Regions of rapid sea ice change : An inter-hemispheric seasonal comparison. **39**: 1–8. doi:10.1029/2012GL050874

Stanley, R. H. R., J. B. Kirkpatrick, N. Cassar, B. A. Barnett, and M. L. Bender. 2010. Net community production and gross primary production rates in the western equatorial Pacific. Global Biogeochem. Cycles **24**. doi:10.1029/2009GB003651

Stroeve, J., and W. N. Meier. 2018. Sea Ice Trends and Climatologies from SMMR and SSM/I-SSMIS, Version 3.doi:10.5067/IJ0T7HFHB9Y6

Teeter, L., R. C. Hamme, D. Ianson, and L. Bianucci. 2018. Accurate Estimation of Net Community Production From O2/Ar Measurements. Global Biogeochem. Cycles **32**: 1163–1181. doi:10.1029/2017GB005874

Tremblay, J. É., S. Bélanger, D. G. Barber, and others. 2011. Climate forcing multiplies biological productivity in the coastal Arctic Ocean. Geophys. Res. Lett. **38**: 2–6. doi:10.1029/2011GL048825

Trull, T. W., P. Jansen, E. Schulz, B. Weeding, D. M. Davies, and S. G. Bray. 2019. Autonomous Multi-Trophic Observations of Productivity and Export at the Australian Southern Ocean Time Series (SOTS) Reveal Sequential Mechanisms of Physical-Biological Coupling. Front. Mar. Sci. **6**: 1–17. doi:10.3389/fmars.2019.00525

Wanninkhof, R. 2014. Relationship between wind speed and gas exchange over the ocean revisited. Limnol. Oceanogr. Methods **12**: 351–362. doi:10.4319/lom.2014.12.351

Wassmann, P., and M. Reigstad. 2011. Future Arctic Ocean Seasonal Ice Zones and Implications for Pelagic-Benthic Coupling. Oceanography **24**: 220–231. doi:10.5670/oceanog.2011.74

Weeding, B., and T. W. Trull. 2014. Hourly oxygen and total gas tension measurements at the Southern Ocean Time Series site reveal winter ventilation and spring net community production. J. Geophys. Res. Ocean. **119**: 348–358. doi:10.1002/2013JC009302

Weiss, R. F., and B. A. Price. 1980. Nitrous oxide solubility in water and seawater. Mar. Chem. **8**: 347–359. doi:10.1016/0304-4203(80)90024-9

Woolf, D. K., and S. A. Thorpe. 1991. Bubbles and the air-sea exchange of gases in near-saturation conditions. J. Mar. Res. **49**: 435–466. doi:10.1357/002224091784995765

Zhou, J., B. Delille, F. Brabant, and J.-L. Tison. 2014. Insights into oxygen transport and net community production in sea ice from oxygen, nitrogen and argon concentrations. Biogeosciences **11**: 5007–5020. doi:10.5194/bg-11-5007-2014